IEEE Access
Multidisciplinary | Rapid Review | Open Access Journal

Received May 31, 2021, accepted June 18, 2021, date of publication June 22, 2021, date of current version June 30, 2021.

Digital Object Identifier 10.1109/ACCESS.2021.3091510

Fast-Slow-Scale Interaction Induced Parallel Resonance and Its Suppression in Voltage Source Converters

RUI MA[1,2], QI QIU[1,2], JÜRGEN KURTHS[3,4], AND MENG ZHAN[1,2], (Member, IEEE)

[1]School of Electrical and Electronic Engineering, Huazhong University of Science and Technology, Wuhan 430074, China
[2]State Key Laboratory of Advanced Electromagnetic Engineering and Technology, Huazhong University of Science and Technology, Wuhan 430074, China
[3]Department Complexity Science, Potsdam Institute for Climate Impact Research, 14473 Potsdam, Germany
[4]Institute of Physics, Humboldt University of Berlin, 10099 Berlin, Germany

Corresponding author: Meng Zhan (zhanmeng@hust.edu.cn)

This work was supported in part by the National Natural Science Foundation of China under Grant 12075091, and in part by the International (Regional) Cooperation and Exchange Program of the National Natural Science Foundation of China [Research on Inter-Organizational Cooperation: NSFC-Deutsche Forschungsgemeinschaft (DFG)] under Grant 11861131011.

ABSTRACT Multi-timescale interaction of power electronics devices, including voltage source converter (VSC), has made the stability and analysis of high penetrating renewable power systems very complicated. In this paper, the impedance model is used to analyze the multi-timescale characteristics and interaction of the VSC. Firstly, the multi-timescale impedance characteristics of VSC are investigated based on the Bode plots. It is found that the slow-timescale (within the DC-link voltage control scale) and fast-timescale (within the AC current control scale) models are separately consistent with the full-order model perfectly within their low- and high-frequency ranges. In addition, there exists a high impedance peak within the intermediate frequency range (roughly from 10 Hz to 100 Hz). Then, the impedance peak is theoretically estimated and explained by the slow-fast-scale impedance parallel resonance through transfer-function diagram analysis. Moreover, it is found that the impedance peak is more related to some outer controllers, such as the alternative voltage control and active power control. Specifically, larger proportional coefficients can greatly suppress the resonance peak. Finally, simulations and experiments are conducted to verify the generality of the multi-timescale characteristics and interaction of the VSC. Hence these findings are not only significant to provide a physical insight into the inner key structure of the impedance of VSC, but also expected to be helpful for controller and parameter design of the VSC.

INDEX TERMS Small-signal stability, multiple time-scale analysis, interaction, parallel resonance, parameter design.

I. INTRODUCTION

With large-scale integration of renewable energies and widespread application of power electronic equipment, the structure of our modern power systems has changed radically. Recently, the emergence of multi-frequency oscillation covering wide frequency bands has seriously threatened the system stability and strongly restricted accommodation of renewable energies around the world [1], [2]. Thereinto, voltage source converter (VSC), usually adopted as a key power electronic device for grid interface of renewable energies, has its intrinsic properties of nonlinear dynamics and multi-timescale interactions of its inner and outer cascading control. The properties make the system analysis harder, compared to the traditional power systems. Therefore, it becomes urgent to study the interaction induced multi-timescale stability problems and uncover the underlying physical mechanism [3], [4].

Effective mathematical modeling is the foundation for system stability studies. So far, the state-space model and the impedance model are two major methods for the small-signal stability analysis [5]–[8]. In the state-space model, usually the modal analysis on state variables is performed, with all detailed information included, such as controller and system parameters. Modal analysis can be used to assess the stability of the system and analyze the couplings through participation factors and sensitivity analysis [9]–[12]. However, it lacks physical insight into the interactions between different

The associate editor coordinating the review of this manuscript and approving it for publication was Feiqi Deng.

controllers (or timescales) in the VSC. In addition, the impacts of specific controllers on the final calculated results of eigenvalues are not apparent. Hence the modal analysis might be difficult to be applied to study the interactions between different timescales and controllers in the VSC.

On the contrary, by focusing on the terminal characteristics of subsystems in the frequency domain, the impedance model of single components (like VSC, MMC and etc.) can be either theoretically obtained or experimentally measured [6], [7], [13]. Especially, how to reveal the multiple frequency coupling mechanisms in MMC through impedance modeling is a difficulty. It becomes convenient to analyze the interaction between different controllers based on the impedance model. The impedance model has been widely studied in different domains including the dq, sequence, $\alpha\beta$, phasor, etc, whose connections and equivalence have been uncovered in [14]–[16]. Several papers have studied the impact of different parameters and controllers on the amplitude-frequency response of impedance of VSC and analyzed the system stability [17]–[21]. Among them, the impact of the phase-locked loop (PLL) based on the dq impedance was analyzed and it was found that the negative resistance effect induced by the PLL was the key factor for system instability [19]. The impact of time delay was also investigated recently via the dq and sequence impedance models. For instance, it was found that a high time delay of the controller can induce an impedance trough around 1kHz [20], [21].

Generally in all previous papers, only single controls or parameters were concentrated and the mutual influence and interaction between different controllers were overlooked. There are several works on system dynamics analysis within each single timescale. For instance, the slow-scale stability problem of VSC was studied in the range of voltage timescale [22]–[25]. It was reported that the oscillations between dozens and hundreds of Hz can be put into the category of current-timescale, by studying a fast-current-scale model. A model reduction methodology based on a state space model was proposed to assess slow-scale dynamics by calculations of eigenvalues and the participating factor [26]. The fast-scale stability of VSC was studied under different parameters' conditions in the range of alternative current timescale [27]. Slow-scale, fast-scale and coexisting bifurcations were studied in a multi-operating-mode photovoltaic-battery system [28], [29]. Obviously, these papers have studied the dynamics of the VSC within the single timescale and missed the influence of interaction between different timescales or controllers.

The interactions between different VSCs have been analyzed through the amplitude-phase modeling and can be quantified by proposed self- and en-stabilizing coefficients in voltage control timescale [30], [31]. What is more, the interaction between double fed induction generator-based wind turbine and synchronous generator can be quantified through self- and en-stabilizing property based on motion equation in electromechanical timescale [32]. However, the quantitative analysis based on the amplitude-phase model is too complex and the interactions between inner and outer controllers (or different timescales) have not been revealed in the electromagnetic timescale. There was little research on the interactions (or couplings) between different timescales based on the impedance model, to the best of our knowledge.

To fill the above these gaps, we will take a closer look at the details of the full-timescale VSC impedance by using multi-timescale analysis. We uncover a novel parallel resonance within the intermediate frequency region and evaluate its influence factors. These findings are expected to be helpful for further system analysis and controller parameters design for the VSC. Extensive simulations and experiments are conducted to verify the theoretical results.

The rest of the paper will be organized as follows. The impedance models within the fast and slow timescales are established and then compared with state-space models in Section II. In Section III, the impedance characteristics of fast- and slow-timescales are shown in the Bode plot and then theoretically analyzed through the order analysis. Section IV is devoted to the intermediate timescale, by focusing on the phenomenon of interaction-induced impedance parallel resonance and the influence factors of the impedance resonance peak. In Section V, we generalize these findings and results to some other outer controllers. Finally, simulation and experimental results are presented in Section VI, and conclusions and discussions are given in Section VII.

II. IMPEDANCE MODELS OF FAST AND SLOW TIMESCALES

The converters in the power electronics systems share some common features. Fig. 1 schematically shows a two-level three-phase VSC tied to the AC grid and its cascaded controls with certain parameters, and the typical parameters are given in Appendix A. The AC grid is represented by an infinite bus with a line inductance (L_g). The impedance of a single VSC in the full-order form has been well derived and studied in literature. Below we like to start from the concrete form of impedance, dissect it carefully, and obtain the corresponding

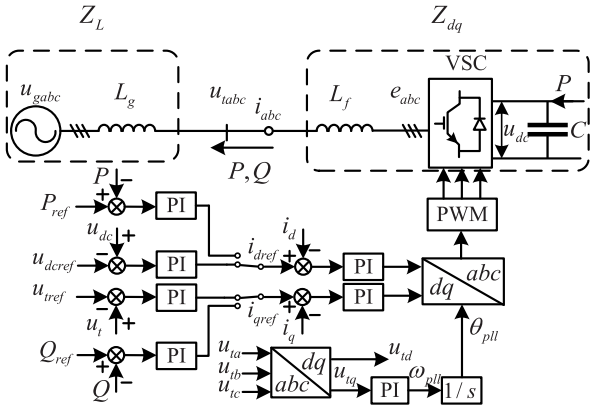

FIGURE 1. Schematic show for a two-level three-phase VSC tied to AC grid and its cascaded controls. The inner alternative current controller (ACC) and different outer controllers such as the direct voltage control (DVC), alternative voltage control (AVC), and power control (PC) are considered. The PLL for the phase output θ_{pll} is used for grid synchronization and VSC control.

impedance models within slow and fast timescales, by using the multi-timescale analysis.

Firstly, let us present the already-existing results of the full-timescale VSC impedance including the alternative current controller (ACC), direct voltage control (DVC), alternative voltage control (AVC), and the PLL for synchronization. According to the detailed derivations of the VSC impedance in Appendix B, all of the transfer functions are in a second-order form. Among them, G_L denotes the open-loop output impedance of the converter, G_{ic} is the current control compensator, and $G_{i,pll}$ and $G_{e,pll}$ indicate the relations between the inductor current (Δi_{dq}) and the internal voltage (Δe_{dq}) in the PLL frame and the terminal voltage (Δu_{tdq}) in the synchronous frame, respectively. G_{iu} and G_{ii} represent the relations between the current reference (Δi_{dqref}) in the PLL frame, and the terminal voltage (Δu_{tdq}) and the inductor current (Δi_{dq}) in the synchronous rotation frame, respectively. For more details, see Appendix B [5], [6], [19].

The output impedance of the VSC can be described by

$$Z_{dq,full} = Z_{a,full}^{-1} Z_{b,full} \tag{1}$$

where

$$\begin{cases} Z_{a,full} = I + G_{ic}G_{i,pll} - G_{e,pll} - G_{ic}G_{iu} \\ Z_{b,full} = G_L + G_{ic} - G_{ic}G_{ii} \end{cases} \tag{2}$$

and I denotes a 2×2 unit matrix.

For a common cascaded control in the VSC, and the bandwidth of the outer voltage controller is usually around five times lower than that of the inner current controller relying on the control design criterion. The power electronics exhibits the intrinsic property of multiple electromagnetic time scales. Essentially based on the knowledge of controller design and understanding of physical equipment, the time scales can be classified into switching (around several kHz), alternative current (around 100 Hz), and dc-link voltage (around 10 Hz) one. The time scale of a phase locking loop (PLL) for synchronization should be considered as between the fast current-control and slow voltage-control scales roughly (10∼100 Hz). As the response speed of switching is very fast, it is usually neglected in the system-level stability analysis.

In this paper we will concentrate on the two electromagnetic time scales mainly: the current-control and voltage-control scales. Though the multi-timescale concepts of the VSC have been proposed in some literature [3], [33], [34], the multi-timescale characteristics and interactions between different controllers (or timescales) have not been compared in detail and investigated from the viewpoint of the frequency domain based on the impedance model.

A. IMPEDANCE MODEL OF SLOW TIMESCALE

Under the DC-link voltage control condition, the dynamic response of the ACC is relatively fast, compared to that of the outer controllers. Thus, the current output of the VSC on the transmission line can be considered equaling the current reference value. In this case, the VSC can be thought as a constant current source and the transmission-line inductance can be regarded as a constant reactance under the working frequency. These assumptions are consistent with [22]–[25]. Therefore, we have

$$\Delta i_{dq}^{c} = \Delta i_{dqref} \tag{3}$$

Furthermore, by considering (A.1), the slow-timescale impedance including the DVC, AVC, and PLL can be written as

$$Z_{dq,slow} = Z_{a,slow}^{-1} Z_{b,slow} \tag{4}$$

where

$$\begin{cases} Z_{a,slow} = G_{i,pll} - G_{iu} \\ Z_{b,slow} = I - G_{ii} \end{cases} \tag{5}$$

The small-signal stability of this impedance model is consistent with that of the state space models and amplitude-phase models established in [23], [34], [35]. Compared with $Z_{a,full}$ and $Z_{b,full}$ in (2), the dynamic behaviors of the current inner controllers and the line inductance are neglected, and the line currents are equal to the current references. Namely, G_{ic} and G_L are neglected.

B. IMPEDANCE MODEL OF FAST TIMESCALE

In contrast, under the current control fast-timescale condition, the action of the outer voltage controllers can be regarded as relatively slow and their outputs can be thought as constants. These assumptions are consistent with [6], [27]. Therefore,

$$\Delta i_{dqref} = 0 \tag{6}$$

Combing it with (A.2), we get

$$\Delta e_{dq}^{c} = -G_{ic}\Delta i_{dq}^{c} \tag{7}$$

which yields the final impedance within the fast timescale including ACC and PLL:

$$Z_{dq,fast} = Z_{a,fast}^{-1} Z_{b,fast} \tag{8}$$

where

$$\begin{cases} Z_{a,fast} = I + G_{ic}G_{i,pll} - G_{e,pll} \\ Z_{b,fast} = G_L + G_{ic} \end{cases} \tag{9}$$

The small-signal stability of this impedance model is consistent with that of the state space models and amplitude-phase models established in [5], [27], [33]. Compared with $Z_{a,full}$ and $Z_{b,full}$ in (2), now the dynamic behaviors of the voltage outer controllers are neglected, and the line current references are set as constants; both G_{iu} and G_{ii} equal zero.

C. SMALL-SIGNAL STABILITY BASED ON IMPEDANCE MODEL

The systems can be transformed into a simplified circuit composed of the two impedance (or admittance) elements [6], where the transfer function diagram of the impedance-based

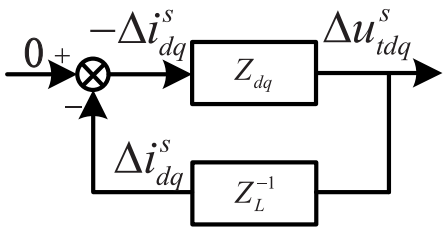

FIGURE 2. Transfer function diagram of the impedance-based source-load system.

source-load system is shown in Fig. 2. The minor loop gain of transfer function can be obtained:

$$H_{open} = Z_L^{-1} Z_{dq} \tag{10}$$

where Z_L denotes the impedance of the load (here is the line inductance in Fig. 1), and Z_{dq} denotes the impedance of the source (here is the VSC in Fig. 1). Consequently, based on this open-loop information, the so-called generalized Nyquist criterion (GNC) can be used to justify system stability, relying on the multi-variable frequency-domain analysis theory.

Accordingly the closed-loop transfer function is

$$G_{closed} = -Z_{dq}(I + Z_L^{-1} Z_{dq})^{-1} \tag{11}$$

Obviously, the system stability can also be judged by its poles.

On the other hand, the system stability can also be determined by a time-domain state space model. The related state space models for the slow-scale, fast-scale, and full-scale are shown in Appendices C, D, and E, respectively. Theoretically, the Smith-McMillan poles of the closed loop transfer function should be equivalent to the eigenvalues calculated from the state matrix due to modern control theory. The calculated results are shown in Tab. 1, where, by comparing the values in the left and right columns, we can see that they fit with each other perfectly.

In addition, by comparing the values on different rows, one can find that the full-scale model does contain the whole information of system while the fast and slow models just contain the information in their frequency range. The inner and outer controllers indeed exhibit the intrinsic property of fast and slow timescales separately. Though the mutual influence of different controllers can be analyzed based on the modal analysis, the multi-timescale characteristics and interactions can be further revealed from the viewpoint of the frequency domain based on the impedance model.

III. CHARACTERISTICS ANALYSIS OF SLOW AND FAST-TIMESCALE IMPEDANCE MODELS

A. COMPARISON OF IMPEDANCES WITHIN FAST, SLOW, AND FULL TIMESCALES

As the first step, we plot the above theoretical results of full, slow, and fast timescale impedances in Figs. 3 and 4 for their amplitude and phase responses, respectively. The frequency varies from 1 Hz to 1000 Hz, which we are interested in. The red solid, blue dashed, and green dot-dashed lines denote full-, fast-, and slow-scale behaviors, respectively. In addition, the values of impedance can also be measured through injecting small-signal voltage (or current) disturbances in MATLAB/Simulink. The measuring impedance values are also superimposed in Fig. 3 and 4 with red markers '×', showing a perfect match with the theoretical results.

Based on these comparisons, obviously the slow-timescale impedance matches with the full-timescale impedance very well within the lower frequency range (roughly lower than 10 Hz), whereas the fast-timescale impedance matches with the full-timescale impedance very well within the higher frequency range (roughly above 100 Hz), except that there is a small visible mismatch in Z_{qd}. This mismatch in high frequency range can be narrowed by decreasing the proportional coefficient of AVC ($k_{p,avc}$) according to the Bode responses, which is discussed in Appendix F.

TABLE 1. Comparison of eigenvalues in state space models and poles of closed-loop transfer functions in impedance models.

	Eigenvalues of state space model	Smith-McMillan poles of closed loop transfer function
Full-scale model	-12.22 $-6.31 \pm j24.41$ $-25.23 \pm j37.71$ $-243.22 \pm j374.13$ $-387.73 \pm j705.16$	-12.22 $-6.31 \pm j24.41$ $-25.23 \pm j37.71$ $-243.22 \pm j374.13$ $-387.73 \pm j705.16$
Slow-scale model	-12.25 $-6.07 \pm j24.87$ $-24.46 \pm j36.04$	-12.25 $-6.07 \pm j24.87$ $-24.46 \pm j36.04$
Fast-scale model	$-22.66 \pm j38.04$ $-214.44 \pm j356.77$ $-422.92 \pm j684.21$	$-22.66 \pm j38.04$ $-214.44 \pm j356.77$ $-422.92 \pm j684.21$

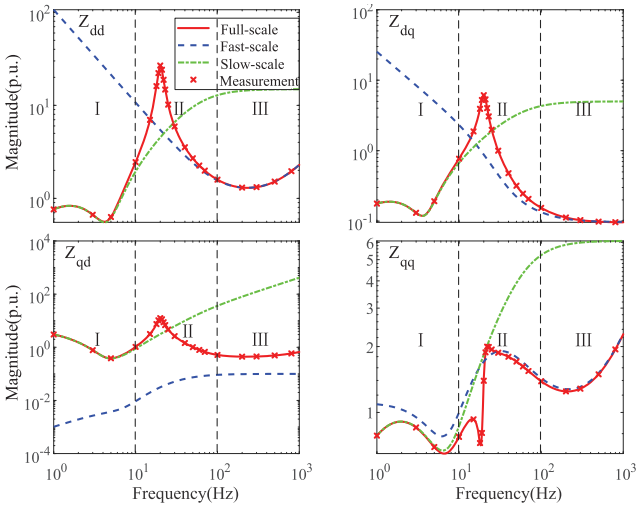

FIGURE 3. Amplitude response of impedances of the VSC within different timescales. The red solid, blue dashed, and green dot-dashed lines denote full-, fast-, and slow-scale behaviors, respectively. In addition, we use red products for the measuring results. Roughly the whole frequency range can be divided by two vertical lines into low (1 ∼ 10 Hz), middle (10 ∼ 100 Hz), and high (100 ∼ 1000 Hz) ones, represented by roman numerals: I, II, and III, respectively.

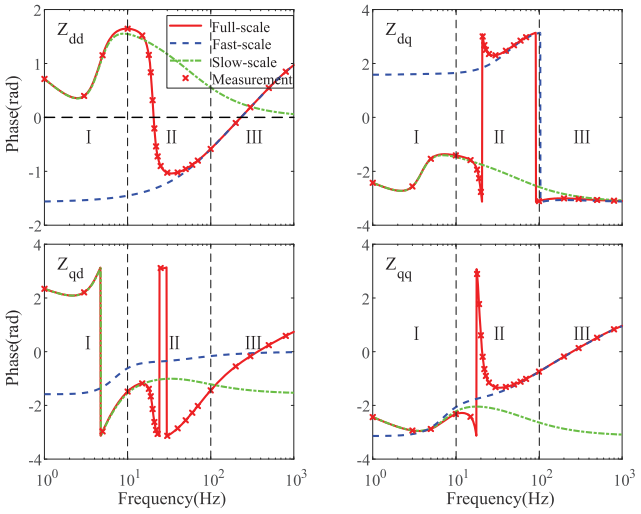

FIGURE 4. Same as Fig. 3 with phase response considered, instead.

In the middle region, they both cannot fit with the full-timescale impedance. Therefore, based on these observations, the whole frequency range can be divided into three ranges in each sub-figures of Fig. 3 and Fig. 4, which are emphasized by roman numerals, I, II, and III. The two crossover frequencies have been indicated by vertical dashed lines. Within the middle frequency region II, both curves of the slow and fast timescale impedances substantially deviate from that of the full-timescale impedance. There is not a smooth transition from the slow to fast timescales. An impedance amplitude peak exists within the II region ($f \approx 20$ Hz) in the amplitude response plots in Fig. 3, accompanying with a discontinuous phase jumping in the phase response plots in Fig. 4. Recalling the impedance trough phenomenon induced by time delay around 1kHz, which was reported recently in [20], [21], one may reasonably infer that the impedance peak and impedance trough can be thought as a unified phenomenon induced by the changing of dominating scale dynamics when a timescale transition happens. The relevant problems of the impedance peak within the intermediate frequency range will be further studied in detail in Section IV.

B. IMPEDANCE APPROXIMATION OF DOMINANT TERMS WITHIN FAST AND SLOW SCALES

So far, we have seen that the VSC impedance characteristics can be well revealed by the model analysis within the low and high frequency ranges. Below we like to get approximative impedances by studying the dominant terms of the full-order model in the limits of low and high frequencies through order analysis. As in the frequency domain $s = j\omega$, in the limit of high frequency, the term with a higher order of s will be dominant. On the contrary, in the limit of low frequency, the term with a lower order of s will be dominant. As $Z_{dq,full}$ in (1) is controlled by $Z_{a,full}$ and $Z_{b,full}$, we can analyze their orders in terms of s and simply keep the dominant terms as our approximation. The analytical result is illustrated in Tab. 2, where $Z_{a,full}$ and $Z_{b,full}$ can be roughly classified into four categories, based on the order s for each item. Directly we have the simplified expressions for the impedances within the lower and higher frequency ranges, respectively,

TABLE 2. Dominated item analysis of $Z_{a,full}$ and $Z_{b,full}$.

	Z_a	Z_b
-2 order (s^{-2})	$G_{ic}G_{i,pll} - G_{ic}G_{iu}$	$-G_{ic}G_{ii}$
-1 order (s^{-1})	$-G_{e,pll}$	G_{ic}
0 order (s^0)	I	—
1 order (s^1)	—	G_L

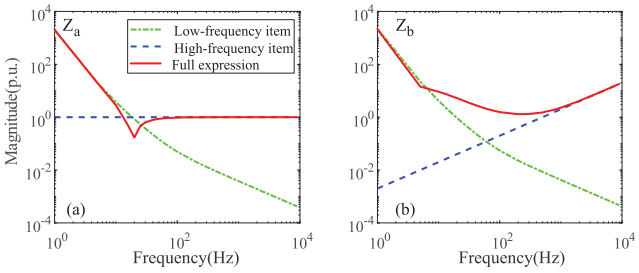

FIGURE 5. Amplitude responses of (a) $Z'_{a,slow}$, $Z'_{a,fast}$, and $Z_{a,full}$, and (b) $Z'_{b,slow}$, $Z'_{b,fast}$, and $Z_{b,full}$. Only their dd components are presented. Clearly the two impedances $Z'_{dq,slow}$ and $Z'_{dq,fast}$ match with $Z_{dq,full}$ within both low and high frequency ranges roughly.

$$Z'_{dq,slow} = (Z'_{a,slow})^{-1} Z'_{b,slow} \tag{12}$$

where

$$\begin{cases} Z'_{a,slow} = G_{i,pll} - G_{iu} \\ Z'_{b,slow} = -G_{ii} \end{cases} \tag{13}$$

and

$$Z'_{dq,fast} = (Z'_{a,fast})^{-1} Z'_{b,fast} \tag{14}$$

where

$$\begin{cases} Z'_{a,fast} = I \\ Z'_{b,fast} = G_L \end{cases} \tag{15}$$

The frequency response of VSC is similar to inductance in high frequency range, which is consistent with our intuition and engineering practice. Comparing these expressions with those of $Z_{dq,slow}$ in (4) and $Z_{dq,fast}$ in (8), one can see that $Z'_{dq,slow}$ and $Z'_{dq,fast}$ have been simplified comparatively, as only the dominant terms have been kept.

To prove this approximation, Fig. 5 shows the amplitude responses of $Z'_{a,slow}$, $Z'_{a,fast}$, and $Z_{a,full}$ in (a), and $Z'_{b,slow}$, $Z'_{b,fast}$, and $Z_{b,full}$ in (b), respectively. Only their dd components are presented. Apparently the low-frequency and high-frequency terms are separately consistent with the full-expression of $Z_{a,full}$ and $Z_{b,full}$ in the slow- and fast-timescale ranges, indicative of the correctness of the above approximation.

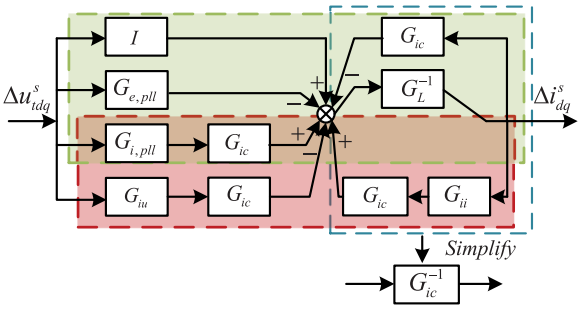

FIGURE 6. Transfer function diagram of the VSC's admittance. The fast-scale (slow-scale) components are given in the top green box (bottom red box). In between, $G_{ic}G_{i,pll}$ serves as their common parts, representing the impact of the PLL. On the right of the diagram, all three branches can be simplified to G_{ic}^{-1}, based on our dominant-order analysis presented in Tab. 2.

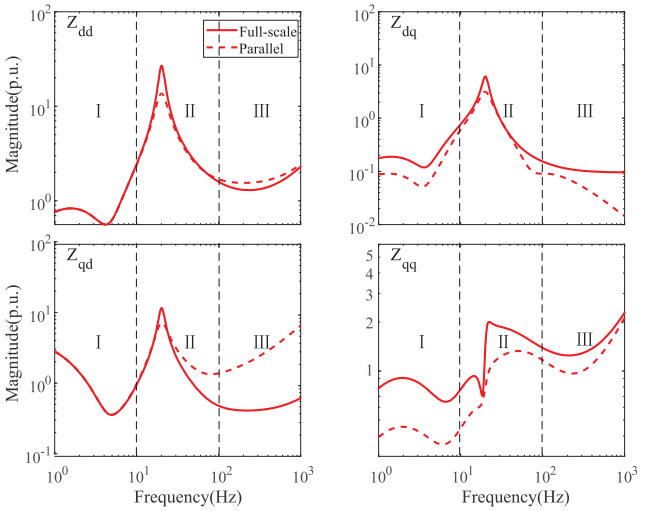

FIGURE 7. Comparison of amplitude response of full-scale impedance (solid line) with that of parallel connection of the fast-scale and slow-scale impedances (dashed line).

IV. CHARACTERISTICS ANALYSIS OF INTERMEDIATE-TIMESCALE IMPEDANCE

In this section, the phenomenon and its physical mechanism of the impedance peak within the middle frequency range will be concentrated. Furthermore, the influences of different controllers and parameters will be investigated.

A. ESTIMATION OF THE IMPEDANCE PEAK's FREQUENCY

Observing that the impedance peak is located at around 20 Hz in Fig. 3, and meanwhile the amplitude response of $Z_{b,full}$ is smooth in Fig. 5(b) and that of $Z_{a,full}$ in Fig. 5(a) shows a rapid drop within the middle frequency range, we can only calculate the extreme point of the dd element of the $Z_{a,full}$ matrix in Fig. 5(a), which can be expressed in (16), as shown at the bottom of the next page.

Let $dZ_{a,full(dd)}(j\omega)/d\omega = 0$, we have

$$\omega_{1,2}^2 = \frac{-4(ac - b^2d^2)}{2(4bd - 2a^2d^2)} \pm \frac{\sqrt{16(ac - b^2d^2)^2 + 4(4bd - 2a^2d^2)6c^2d^2}}{2(4bd - 2a^2d^2)} \quad (17)$$

where $a = k_{p,cc}k_{p,dvc}$, $b = (k_{i,cc}k_{p,dvc} + k_{p,cc}k_{i,dvc})$, $c = k_{i,cc}k_{i,dvc}$, and $d = I_{d0}/C$. This yields the peak frequency at 19.73 Hz, which is consistent with the aforementioned numerical observation in Fig. 3. We can also see that this peak frequency is determined by the control parameters of the ACC and DVC, and the DC capacitor, meaning that the peak is contributed by an interplay of both fast- and slow-scale controllers. Further physical explanation and extensive plots under different parameters will show that the impedance peak is a generic phenomenon.

B. PHYSICAL MECHANISM OF THE IMPEDANCE PEAK

Further efforts should be made for uncovering the mechanism of the impedance peak. For this purpose, we examine the detailed transfer function diagram in the full-timescale admittance of the VSC, $Y_{dq,full}$, in Fig. 6. This is consistent with the form of $Z_{dq,full}$ in (1). Basically its left and right parts represent the contributions of $Z_{a,full}$ and $Z_{b,full}^{-1}$, respectively. In view of the top and bottom parts, the top green box and bottom red box separately represent the contributions within the slow and fast scales. In between, $G_{ic}G_{i,pll}$ serves as their common part, representing the impact of the PLL. In addition, the whole right part in Fig. 6 for $Z_{b,full}^{-1}$ can be simplified to G_{ic}^{-1}, as the s^{-1}-order item of $Z_{b,full}$, G_{ic}, is dominant within the intermediate frequency range in Tab. II. Therefore, we have the admittance expressions under different timescales,

$$\begin{cases} Y_{dq,full} = G_{ic}^{-1}(I + G_{ic}G_{i,pll} - G_{e,pll} - G_{ic}G_{iu}) \\ Y_{dq,slow} = G_{ic}^{-1}(G_{ic}G_{i,pll} - G_{ic}G_{iu}) \\ Y_{dq,fast} = G_{ic}^{-1}(I + G_{ic}G_{i,pll} - G_{e,pll}) \end{cases} \quad (18)$$

for $Y_{dq,full}$, $Y_{dq,slow}$, and $Y_{dq,fast}$ representing admittances within the full, slow, and fast timescales, respectively. Furthermore, based on that $G_{ic}G_{i,pll}$ (serving as a s^{-2}-order item in Tab. II) is relatively small within the intermediate frequency range, we immediately have:

$$Y_{dq,full} \approx Y_{dq,slow} + Y_{dq,fast} \quad (19)$$

which indicates that within the middle frequency region, the full-scale admittance can be viewed as a sum of the slow-scale and the fast-scale admittance, and hence from the perspective of impedance, the full-scale impedance can be viewed as parallel connection of the slow-scale and fast-scale impedance. Last we supplement that as parallel impedance is considered, it is more convenient to study it in the form of admittance summation, as we have done in the analysis of the transfer function control diagram in Fig. 6.

To check this point, Figs. 7 and 8 show the comparison of amplitude-phase response of the original full-timescale impedance $Z_{dq,full}$ (red solid line) with that of the parallel impedance of the fast-scale and slow-scale impedances,

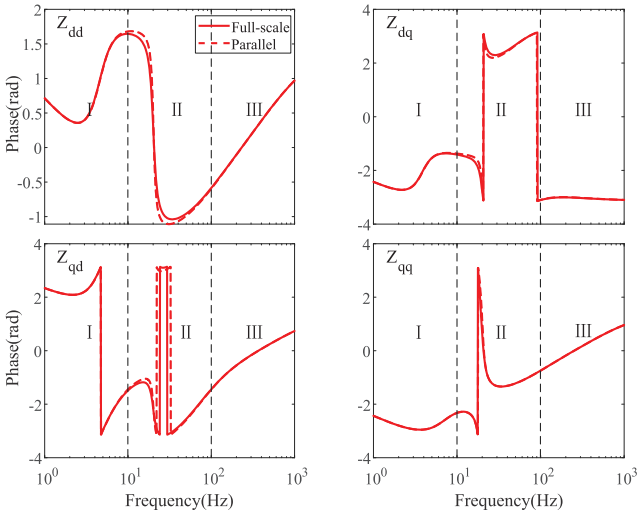

FIGURE 8. Same as Fig. 7 with phase response considered, instead.

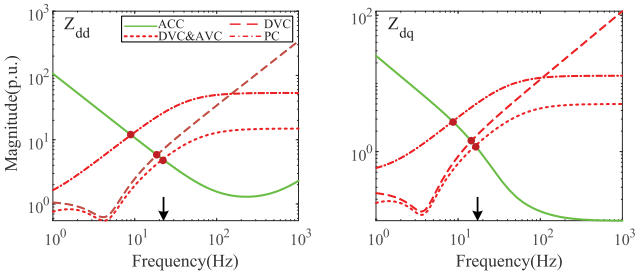

FIGURE 9. Amplitude response of impedance (Z_{dd} and Z_{dq}) for different outer controllers to examine the parallel resonance mechanism. Green solid line is for the ACC fast-scale impedance. Red dotted, dashed, and dot-dashed lines are for the DVC & AVC, DVC, and PC outer-control slow-scale impedances.

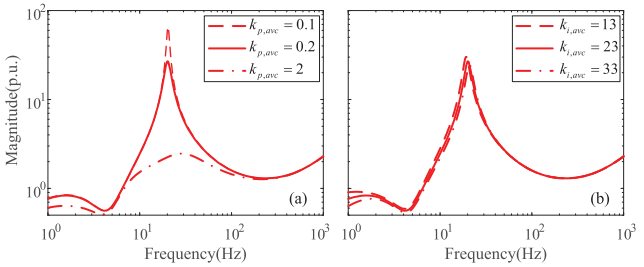

FIGURE 10. Amplitude responses of impedance, Z_{dd}, under different PI parameters of the AVC: (a) $k_{p,avc} = 0.1, 0.2, 2$ (b) $k_{i,avc} = 13, 23, 33$, which are represented by dashed, solid, and dot-dashed lines, respectively.

$Z_{dq,fast}$ and $Z_{dq,slow}$ (red dashed line). It can be seen that their difference of amplitude within the middle frequency region is small and their phases are almost the same.

Next we can find that the different characteristics of slow- and fast-scale impedance lead to this impedance peak, which can be named after *parallel resonance peak*. Recall the phenomenon of phase jumping in the phase response in Fig. 4, either from positive to negative in Fig. 4(a) (Z_{dd}) or from negative to positive in Figs. 4(b)-4(d). This means that around the impedance peak, the electrical characteristics of Z_{dd}, Z_{dq}, Z_{qd}, and Z_{qq} of the fast- and slow-scale impedances are always opposite, i.e., one is inductive (or capacitive) and the other is capacitive (or inductive). Combining this with the parallel impedance rule, we understand that a parallel resonance occurs under the parallel connection of fast and slow-scale impedances. This is similar to the well-known RLC parallel resonance in electrical circuits. Finally, to make this mechanism clearer, we plot the amplitude response of the current-scale ACC impedance (solid curve) and the voltage-scale impedance under the DVC & AVC (dashed curve) in Fig. 9, where the intersection of these two curves is just located at $f \approx 20$ Hz (guided by an arrow), indicative of the occurrence of the parallel resonance. The appearance of this parallel resonance within the middle frequency region may play an active role in stability of VSC systems.

C. IMPACT OF CONTROLLERS ON THE PARALLEL RESONANCE PEAK AND THE SYSTEM's STABILITY

The impacts of the parameters of the AVC, DVC, ACC, PLL and current decouple terms on the resonance peak are investigated below. It should be noted that as the figures of all Z_{dd}, Z_{dq}, Z_{qd}, and Z_{qq} are similar, only the amplitude responses of Z_{dd} will be presented. In addition, the dominated eigenvalues (determined by the sensitivities and participation factors) will be studied and compared under different proportional and integral (PI) parameters, which should be useful for further parameter design.

1) IMPACT OF AVC's PARAMETERS

The amplitude responses of the impedance Z_{dd} under different PI coefficients of the AVC are shown in Fig. 10. It can be seen that the resonance peak decreases dramatically with the increase of $k_{p,avc}$ in Fig. 10(a), while it almost remains unchanged with the increase of $k_{i,avc}$ in Fig. 10(b). Hence the resonance peak can be suppressed by increasing $k_{p,avc}$.

The AVC mainly influences the real eigenvalue, i.e. -12.22 in Tab. 1, according to the participation factors. The dominated eigenvalues under different parameters are calculated and illustrated in Tab. 3. It can be found that the eigenvalue keeps away from the imaginary axis with the increase of $k_{i,avc}$ and the decrease of $k_{p,avc}$, so a higher $k_{i,avc}$ and a smaller $k_{p,avc}$ are beneficial for the system small-signal stability.

2) IMPACT OF DVC's PARAMETERS

Correspondingly, the amplitude responses of impedance Z_{dd} under different PI coefficients of the DVC are shown

$$Z_{a,full(dd)}(s) = 1 + \frac{I_{d0}[k_{p,cc}k_{p,dvc}s^2 + (k_{i,cc}k_{p,dvc} + k_{p,cc}k_{i,dvc})s + k_{i,cc}k_{i,dvc}]}{Cs^3} \tag{16}$$

TABLE 3. The dominated eigenvalues with different PI parameters of AVC.

I \ P	0.1	0.2	2
13	-7.66	-7.25	-3.65
23	-12.82	-12.22	-6.42
33	-17.38	-16.65	-9.11

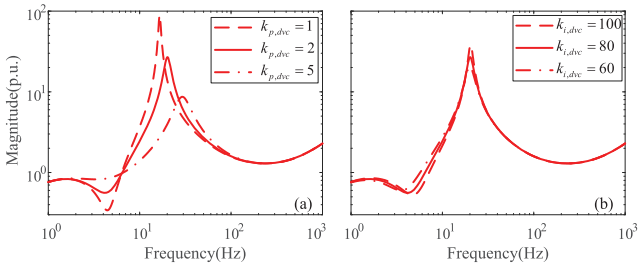

FIGURE 11. Amplitude responses of impedance (Z_{dd}) under different PI parameters of the DVC: (a) $k_{p,dvc} = 1, 2, 5$. (b) $k_{i,dvc} = 100, 80, 60$, which are represented by dashed, solid, and dot-dashed lines, respectively.

TABLE 4. The dominated eigenvalues with different PI parameters of DVC.

I \ P	1	2	5
100	$-3.08 \pm j24.47$	$-6.27 \pm j28.86$	$-17.80 \pm j25.77$
80	$-2.98 \pm j24.90$	$-6.31 \pm j24.41$	$-20.43 \pm j20.60$
60	$-2.99 \pm j21.89$	$-6.64 \pm j21.28$	$-21.43 \pm j14.06$

in Fig. 11. It can be seen that the resonance peak decreases with the increase of $k_{p,dvc}$ in Fig. 11(a), while it changes a little with the decrease of $k_{i,dvc}$ in Fig. 11(b). Therefore, it can be gotten that the impact of the DVC on the resonance peak is relatively smaller than that of the AVC.

Similarly, the DVC mainly influences the slow-scale eigenvalues, i.e. $-6.31 \pm j24.41$ in Tab. 1, according to the participation factors. The dominated eigenvalues are calculated and concluded in Tab. 4 under different parameters. It can be seen that the real part of eigenvalues keeps away from the imaginary axis with the increase of $k_{p,dvc}$ and decrease of $k_{i,dvc}$, so a higher $k_{p,dvc}$ and a smaller $k_{i,dvc}$ are beneficial for the system small-signal stability.

3) IMPACT OF ACC's PARAMETERS

The amplitude response of impedance Z_{dd} under different PI coefficients of ACC are shown in Fig. 12. It can be seen that the resonance peak decreases dramatically with the increase of $k_{p,cc}$ in Fig. 12(a), while it almost keeps unchanged with the increase of $k_{i,cc}$ in Fig. 12(b). Hence the resonance peak can be suppressed by increasing $k_{p,cc}$, corresponding to a larger bandwidth of the ACC.

Now for the ACC, it mainly influences two fats-scale eigenvalues, i.e. $-387.73 \pm j705.16$ and $-243.22 \pm j374.13$ in Tab. 1, according to the participation factors. The dominated eigenvalues under different parameters are shown in Tab. 5. It can be seen that one pair of eigenvalues approaches the

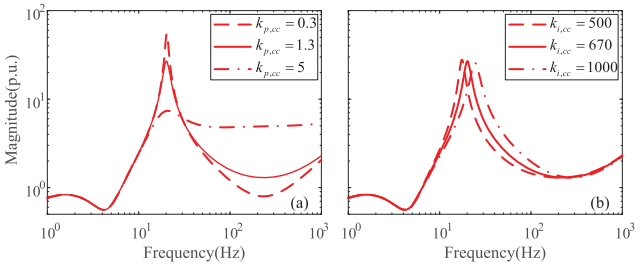

FIGURE 12. Amplitude responses of impedance (Z_{dd}) under different PI parameters of the ACC: (a) $k_{p,cc} = 0.3, 1.3, 5$. (b) $k_{i,cc} = 500, 670, 1000$, which are represented by dashed, solid, and dot-dashed line, respectively.

TABLE 5. The two dominated eigenvalues under different PI parameters of ACC.

I \ P	0.3	1.3	5
500	$-81.65 \pm j672.38$ $-38.45 \pm j394.83$	$-417.85 \pm j627.73$ $-214.80 \pm j283.82$	$-2408 \pm j946.5$ $-101.9 \pm j16.9$
670	$-77.00 \pm j742.33$ $-43.22 \pm j480.85$	$-387.73 \pm j705.16$ $-243.22 \pm j374.13$	$-2371.2 \pm j948.5$ $-138.9 \pm j22.27$
1000	$-71.07 \pm j853.52$ $-49.26 \pm j626.48$	$-351.57 \pm j832.06$ $-281.33 \pm j525.11$	$-2296.9 \pm j954.1$ $-213.3 \pm j35.2$

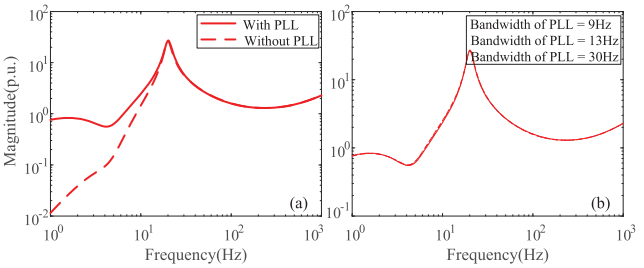

FIGURE 13. Amplitude responses of impedance Z_{dd} by considering the different effects of the PLL: with (solid line) and without the PLL (dashed line) (a), and different bandwidths of the PLL under 9, 13, and 30 Hz, represented by the dashed, solid, and dot-dashed lines, respectively (b).

imaginary axis and the other one keeps away from the imaginary axis with the increasing of $k_{i,cc}$. For the $k_{p,cc}$, one pair of eigenvalues continuously keeps away from the imaginary axis with the increasing of $k_{p,cc}$, and the other one keeps away from the imaginary axis firstly and then approaches it with the increase of $k_{p,cc}$. Though the changing trends of $k_{i,cc}$ and $k_{p,cc}$ are not the same, generally higher $k_{i,cc}$ and $k_{p,cc}$ are beneficial for the small-signal stability of system, which is consistent with [27].

4) IMPACT OF PLL

The amplitude responses of impedance Z_{dd} with and without PLL are compared and shown in Fig. 13(a). The corresponding results under different bandwidths of the PLL are shown in Fig. 13(b). It can be seen that the influence of PLL is only limited on relatively lower frequency range, i.e., smaller than 15 Hz. Meanwhile, the amplitude response of impedance Z_{dd} almost remains unchanged with the change of the bandwidth of PLL [e.g., 9 Hz, 13 Hz and 30 Hz in Fig. 13(b)]. As a result,

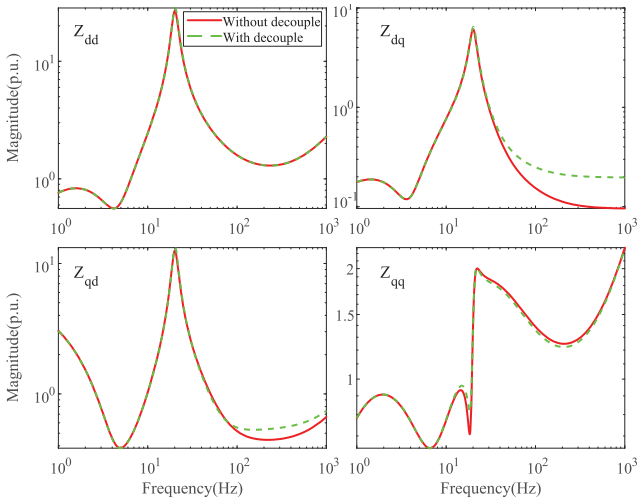

FIGURE 14. Amplitude responses of the impedance without (red solid line) and with (green dashed line) current decouple terms.

it can be concluded that the influence of PLL on the resonance peak is negligible.

5) IMPACT OF THE CURRENT DECOUPLE TERMS

The amplitude responses of the impedance without and with the current decouple terms are compared and shown in Fig. 14. It can be seen that there is only a small mismatch in the high frequency range. Therefore, the current decouple terms have little influence on the characteristics of the impedance. Meanwhile, it can be found that the amplitude responses without and with the current decouple terms are very similar in the intermediate frequency range. Consequently, the impacts of the current decouple terms on the resonance peak can be neglected.

In conclusion, the influence of the current decouple items and the PLL on the resonance peak can be neglected. On the contrary, all the controllers' proportional coefficients have a great impact on the resonance peak. For instance, for the ACC, a larger $k_{p,cc}$ corresponding to a larger bandwidth of the ACC can relieve the resonance peak. Compared with the DVC, the impact of the AVC on the resonance peak is relatively larger. A larger $k_{p,avc}$ corresponding to a larger bandwidth of the AVC can suppress the resonance peak substantially; this point may not be consistent with some design principles and intuition.

V. RESULTS FOR OTHER OUTER CONTROLLERS

In this section, we will present some results for other forms of outer controllers, to further show that the peak phenomenon is generic. Similarly, the impacts of different parameters on the resonance peak will be investigated.

A. PARALLEL IMPEDANCE RESONANCE FOR OTHER OUTER CONTROLLERS

As the first case, we neglect the AVC and consider the DVC only. Under this situation, the q-axis current reference should be set to constant, i.e.,

$$\Delta i_{qref} = 0 \tag{20}$$

Hence the impedance expression is the same as in (2), and it can be obtained by using the new G_{iu} in Appendix G.

For the second case, we consider the active and reactive power control (PC), and it can be gotten that:

$$\begin{cases} i_{dref} = H_p(P_{ref} - P) \\ i_{qref} = H_q(Q_{ref} - Q) \end{cases} \tag{21}$$

where $H_p = k_{p,p} + k_{i,p}/s$ and $H_Q = k_{p,q} + k_{i,q}/s$. Similarly, the impedance can be derived by linearizing (21) and updating the forms of G_{iu} and G_{ii} in Appendix H.

For these two different cases, we find that all aforementioned findings persist, including three frequency regions for slow, intermediate, and fast timescales with an impedance peak in the intermediate timescale, except that the specific values may change. For example, different from the $1 \sim 10$ Hz, $10 \sim 100$ Hz, and $100 \sim 1000$ Hz in the AVC & DVC for the frequency ranges of the slow, intermediate, and fast timescales, respectively, here they become $1 \sim 6$ Hz, $6 \sim 100$ Hz, and $100 \sim 1000$ Hz in the first case, and $1 \sim 3$ Hz, $3 \sim 60$ Hz, and $60 \sim 1000$ Hz in the second case. In addition, the resonance frequency also shows a system dependence. Different from $f \approx 20$ Hz in the AVC & DVC, here it becomes $f \approx 18$ Hz in the first case and $f \approx 9$ Hz in the second case. For illustration, the results for these two cases are superimposed in Fig. 9, where the parallel resonance corresponding to the intersection of two curves of slow-scale and fast-scale impedances is unchanged. This demonstrates that the mutual interaction between inner and outer controllers with the form of parallel resonance is generic and robust, irrespective of the concrete forms of controllers.

B. IMPACT OF POWER CONTROLLERS' PARAMETERS ON RESONANCE PEAK

1) THE IMPACT OF ACTIVE POWER CONTROLLER

The amplitude responses of the impedance of the VSC under different proportional and integral coefficients of the active power control are also studied. The results of Z_{dd} are shown in Fig. 15(a) and (b), where $(k_{p,p} = 0.01, 0.02, 0.3)$ and $(k_{i,p} = 3, 5, 10)$, respectively. It can be seen that the parallel resonance peak changes dramatically with the increase of $k_{p,p}$, whereas the resonance frequency only moves right slightly with the increase of $k_{i,p}$. Clearly the resonance peak can be greatly suppressed by increasing $k_{p,p}$.

2) THE IMPACT OF REACTIVE POWER CONTROLLER

The amplitude responses of impedance for different PI coefficients of the reactive power control are also studied. Fig. 16(a) and (b) show the results for $(k_{p,q} = 0.02, 0.3, 1)$ and $(k_{i,q} = 3, 5, 10)$, respectively. It can be seen that the resonance peak changes slightly with the change of $k_{p,q}$. Similarly, $k_{i,q}$ also has a little influence. Comparatively the

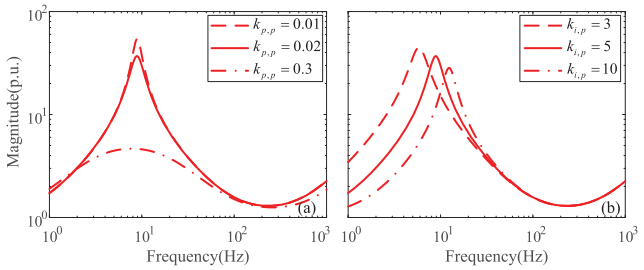

FIGURE 15. Amplitude responses of impedance Z_{dd} under different proportional and integral coefficients of the active power controller: (a) $k_{p,p} = 0.01, 0.02, 0.3$, and (b) $k_{i,p} = 3, 5, 10$, respectively.

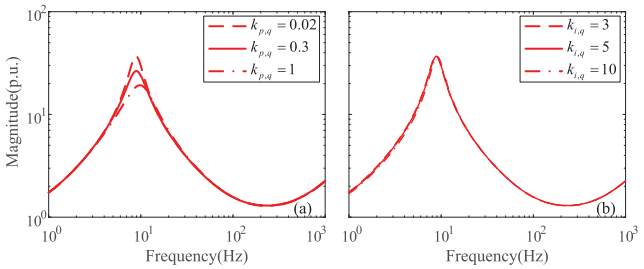

FIGURE 16. Amplitude response of impedance Z_{dd} under different PI parameters of the reactive power controller: (a) $k_{p,q} = 0.02, 0.3, 1$, and (b) $k_{i,q} = 3, 5, 10$, respectively.

impact of the reactive power controller is smaller than that of the active power controller.

To sum up, based on these observations and comparisons, we know that a larger $k_{p,p}$ can relieve the resonance peak substantially while $k_{p,q}$ has a little influence on it. In addition, both the integral coefficients of the power controllers ($k_{i,p}$ and $k_{i,q}$) have a limited influence.

VI. SIMULATION AND EXPERIMENTAL VERIFICATION

A. SIMULATION RESULTS

In our study, a series of simulations have been conducted to verify the impact of interaction of different timescales on the system small-signal stability. Four examples are illustrated in Fig. 17, which show the system unstable situations under different parameters with different oscillation frequencies. Meanwhile, the GNC has also been applied to examine the system stability for comparison. Correspondingly, Tab. 3 summarizes the dominating eigenvalues and critical parameters that are calculated from the reduced-order and full-order models by changing the PI parameters. We use a blank cell to represent that the corresponding critical mode does not exist with the change of the corresponding parameter. Cases 1 and 2 illustrate the fast- and slow-scale modes, respectively, while cases 3 and 4 illustrate the intermediate-scale modes which are both influenced by fast and slow timescales.

Case 1 Low-Frequency Mode: We tune the proportional coefficient in the slow-scale DVC. By decreasing $k_{p,dvc}$ to 0.18, the system becomes unstable and begins oscillating at 4 Hz; the time series and frequency spectrum are shown in Figs. 17(a) and 17(b). Based on Tab. 3, one can see that the critical parameters and the dominated modal frequency in the reduced-order and full-order models are very close.

TABLE 6. Dominated Eigenvalues and Critical Parameters Tuned in Reduced-order and Full-order Models.

	Full-scale model	Slow-scale model	Fast-scale model
Case 1 4Hz	$k_{p,dvc} = 0.18$ $(0 \pm j25.21)$	$k_{p,dvc} = 0.29$ $(0 \pm j25.40)$	—
Case2 118Hz	$k_{p,cc} = 0.11$ $k_{i,cc} = 1250$ $(0.6 \pm j726.8)$	—	$k_{p,cc} = 0.06$ $k_{i,cc} = 1250$ $(0.1 \pm j720.7)$
Case3 90Hz	$k_{p,cc} = 0.11$ $k_{i,cc} = 850$ $(0 \pm j565.0)$	—	$k_{p,cc} = 0.11$ $k_{i,cc} = 168$ $(0 \pm j165.9)$
Case4 99Hz	$k_{i,avc} = 834$ $k_{p,avc} = 0.08$ $(0.13 \pm j625.53)$	—	—

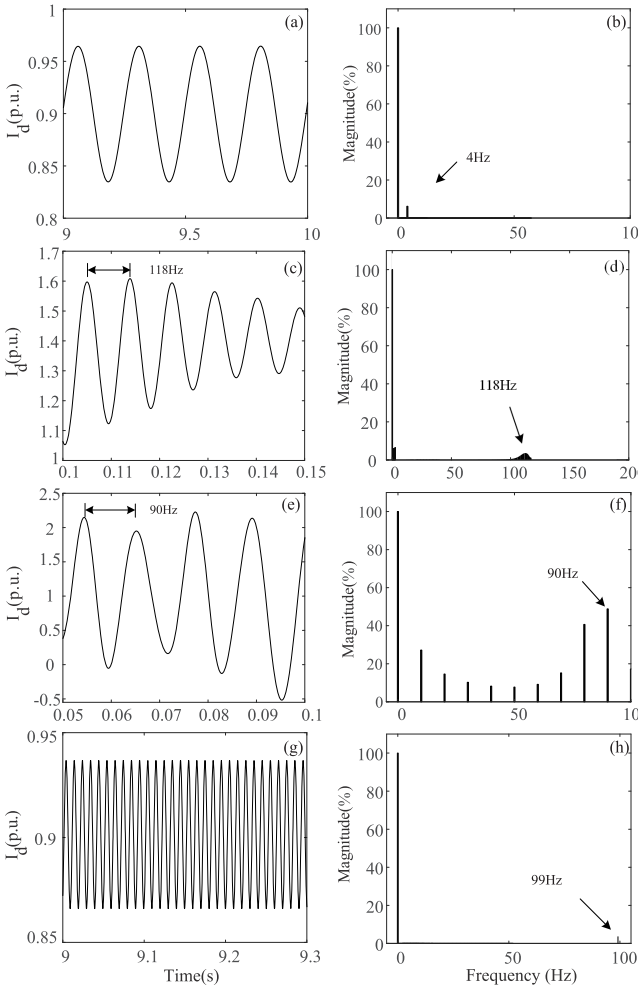

FIGURE 17. Time series (left column) and frequency spectrum (right column) analyses for unstable states under different parameters for the cases 1-4, from top to bottom.

Therefore, for low-frequency oscillations, the slow-scale reduced-order model can indeed catch the dominant system behavior.

Case 2: High-frequency mode. Now we change the proportional coefficient of the ACC. By decreasing $k_{p,cc}$ with a fixed $k_{i,cc} = 1250$, the system becomes unstable and begins oscillating at 116 Hz. In Fig. 17(c) and (d), the parameters

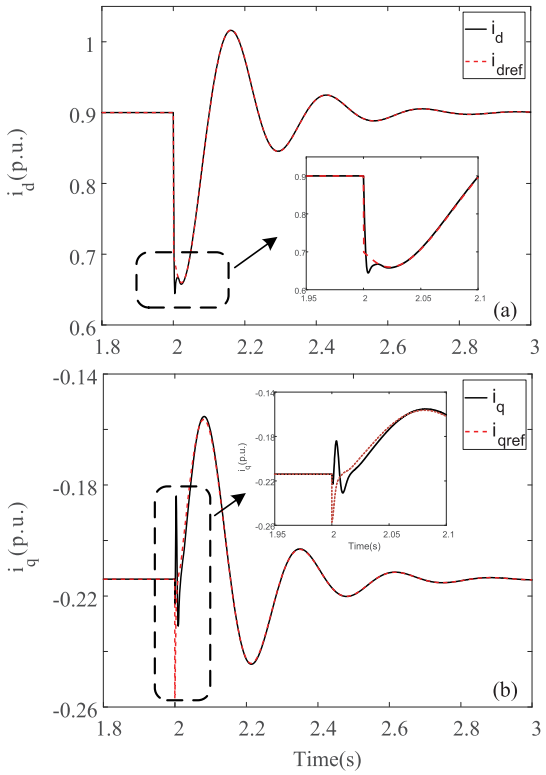

FIGURE 18. Tracking performance for (a) i_d versus i_{dref}, and (b) i_q versus i_{qref}.

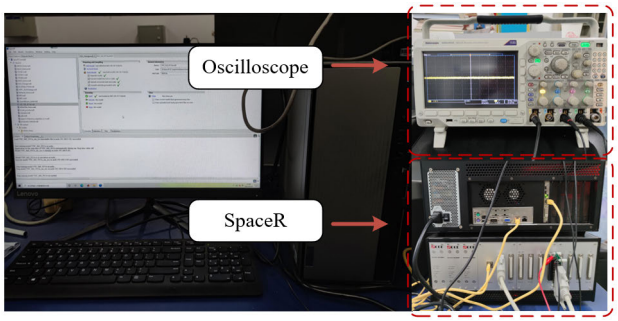

FIGURE 19. Experimental platform based on the SpaceR.

($k_{p,cc} = 0.16$ and $k_{i,cc} = 1250$) for a critically stability are chosen. Again it can be seen that the critical parameters and the dominated modal frequency in the reduced-order and full-order models are close, meaning that for high-frequency oscillations, the full-scale model can be replaced by the fast-scale one.

Case 3: Intermediate frequency mode one. This mode is motivated by changing the integral coefficient of the ACC. Decreasing $k_{i,cc}$ to 850 with a fixed $k_{p,cc} = 0.11$, the system becomes unstable and starts oscillating at 89 Hz. The results are shown in Tab. 3 and Fig. 17(e) and (f). It can be seen that now this unstable mode cannot be accurately predicted by the fast-scale model. Meanwhile, it cannot be observed by tuning the corresponding parameters in the slow-scale model.

Case 4: Intermediate frequency mode two. As the fourth case, we change the integral coefficient of the AVC. By increasing $k_{i,avc}$ to 835, the system begins becoming

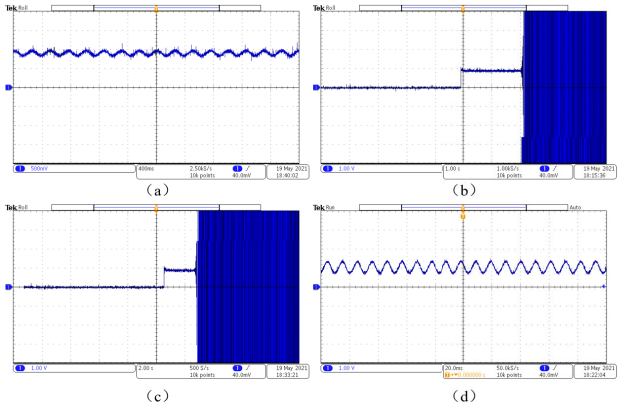

FIGURE 20. (a)-(d) Time series of i_d under different parameters which are same as the simulations in cases 1-4.

unstable and oscillating at 99 Hz. The corresponding results are shown in Tab. 3 and Fig. 17(g) and (h). Now this unstable mode cannot be found in the two reduced-order models by tuning $k_{i,avc}$ solely any more. Based on these observations and comparisons, one understands that the reduced-order models cannot fully reflect the system dynamics, if intermediate frequency oscillations are considered.

Moreover, the tracking performance of i_d versus i_{dref}, and i_q versus i_{qref} is tested. As one example, a small-signal disturbance for the DC-link voltage u_{dc} increasing from 1.0 p.u. to 1.1 p.u. at 2 s, and the corresponding time series of i_d and i_q are shown in Fig. 18. It can be seen that the errors between reference values and measured values are small. Therefore, the tracking performance of the controllers can be thought as good.

B. EXPERIMENTAL RESULTS

The Hardware-in-loop experiments based on the SpaceR are applied for further verification. The SpaceR is a real-time simulation platform, including one part that simulates the AC grid with an equivalent line impedance, and the other one that simulates the VSC, which is shown in Fig. 19. The experimental parameters are the same as those of simulations for cases 1-4. The corresponding time series of i_d measured by oscilloscope are shown in Fig. 20. Among them, Fig. 20(a) and (b) show the fast- and slow-scale modes, respectively, whereas Fig. 20(c) and (d) illustrate the intermediate-scale modes. From the time series measured by oscilloscope, it can be seen that the oscillation frequencies of case 1 and 4 are 4Hz and 99Hz, respectively, which is consistent with the above simulations. Correspondingly for cases 2 and 3 [i.e. Fig. 20(b) and (c)], the systems are unstable, and the systems diverge too quickly to determine their oscillation frequencies. To sum up, these experimental results are consistent with the above simulations.

VII. CONCLUSION AND DISCUSSIONS

In conclusion, we have investigated the impedance characteristics and interaction of the VSC based on the multi-timescale decomposition analysis. It has been found

that the slow-timescale and fast-timescale impedance models are separately consistent with the full-order impedance model within their low- and high-frequency ranges. Meanwhile, there exists a novel intermediate frequency range (roughly from 10 Hz to 100 Hz) with an impedance peak. We discover that the impedance peak is caused by a parallel resonance between the inner and outer controllers. Furthermore, the influence parameters of the impedance peak are explored fully and it is found that the peak can be suppressed by increasing the proportional coefficients of the AVC ($k_{p,avc}$), the active PC ($k_{p,p}$) and the ACC ($k_{p,cc}$). Simulation and experimental results under different controllers and system parameters verify these theoretical analyses. All these findings are expected to be not only helpful for a physical insight into the multi-timescale interaction in the VSC, but also useful for controller design and system analysis of power-electronic-dominated power systems.

For discussion, although the impedance model of a single VSC has been well developed before, it remains a great challenge to generalize it to study multi-converter stability and solve wide-frequency-band oscillation problems. Therefore, it is very necessary and important to deep into the inner back-bone structure of impedance, as what we have done in the present work. The findings of multi-scale decomposition and parallel impedance resonance in the paper are significant to better understand full-order impedance in a physical perspective. Furthermore, they might be helpful for system-level analysis of multi-converter systems. In particular, as sub-synchronous and super-synchronous oscillations around the working frequency have been a serious problem in power electrical engineering recently, the parallel impedance resonance within the middle frequency range (from 10Hz to 100Hz) might be highly relevant. In addition, the multi-timescale analyses have been conducted solely on the impedance models within the small signal category in this paper. Some nonlinear multi-timescale characteristics and interactions should be studied further [36], [37]. Moreover, there are some other interesting problems, such as the influences of uncertainties in system parameters on the interaction, and possible application of the impedance model in some advanced controllers including model predicted controller, robust controller, non-linear controller, etc. It is notable that the impedance analysis method can be used for small-signal stability analysis, not for large-signal stability analysis.

APPENDIX.

A. SYSTEM PARAMETERS

System parameters: S_b =2 MW, U_b = 690 V (phase to phase rms value), $f_1 = 50$ Hz (1.0$p.u.$), $\omega_1 = 2\pi f_1$ (1.0$p.u.$), $L_f = 0.1\ p.u.$, $C = 0.1\mu F$, $U_g = 1.0\ p.u.$, $U_t = 1.0\ p.u.$, $U_{dc} = 1.0\ p.u.$ and $L_g = 0.5\ p.u.$. Controller parameters: (1) ACC: $k_{p,cc} = 1.3$, $k_{i,cc} = 670$. (2) PLL: $k_{p,pll} = 50$, $k_{i,pll} = 2000$. (3) AVC: $k_{p,avc} = 0.2$, $k_{i,avc} = 23$. (4) DVC: $k_{p,dvc} = 2$, $k_{i,dvc} = 80$. (5) Active PC: $k_{p,p} = 0.02$, $k_{i,p} = 5$. (6) Reactive PC: $k_{p,q} = 0.02$, $k_{i,q} = 5$. Steady-state values: $e_{d0} = 1.02\ p.u.$, $e_{q0} = 0.09\ p.u.$, $\varphi_1 = 0.47\ rad$, $i_{d0} = 0.90\ p.u.$ and $i_{q0} = -0.21\ p.u.$.

The impacts of the PI parameters on the small-signal stability of the system are discussed in Section IV, which can be used for further parameter design.

B. DQ-IMPEDANCE MODEL WITH ACC, PLL, AVC & DVC

The dynamic equation of VSC in the AC side is given by

$$G_L \Delta i^s_{dq} = \Delta e^s_{dq} - \Delta u^s_{tdq} \tag{A.1}$$

where $G_L = \begin{bmatrix} sL_f & -\omega_1 L_f \\ \omega_1 L_f & sL_f \end{bmatrix}$ denotes the open-loop output impedance of VSC.

The variable s is used as a Laplacian operator, while the superscript 's' stands for the xy synchronous rotation frame. The internal voltage references obtained from the ACC is

$$\Delta e^c_{dq} = G_{ic} \Delta i_{dqref} - G_{ic} \Delta i^c_{dq} \tag{A.2}$$

where $G_{ic} = \begin{bmatrix} H_{ic} & 0 \\ 0 & H_{ic} \end{bmatrix}$. The ACC compensator transfer function is $H_{ic} = k_{p,cc} + k_{i,cc}/s$, where $k_{p,cc}$ and $k_{i,cc}$ are the proportional and integral gains of the ACC.

The superscript 'c' represents variable in the PLL coordinate. The internal voltage and output current in the xy synchronous rotation frame are connected with those in the PLL coordinate:

$$\begin{cases} \Delta e^s_{dq} = G_{e,pll} \Delta u^s_{tdq} + \Delta e^c_{dq} \\ \Delta i^c_{dq} = G_{i,pll} \Delta u^s_{tdq} + \Delta i^s_{dq} \end{cases} \tag{A.3}$$

$$G_{e,pll} = \begin{bmatrix} 0 & -e^s_{q0} \\ 0 & e^s_{d0} \end{bmatrix} G_{pll} \quad G_{i,pll} = \begin{bmatrix} 0 & I^s_{q0} \\ 0 & -I^s_{d0} \end{bmatrix} G_{pll} \tag{A.4}$$

where $G_{i,pll}$ and $G_{e,pll}$ indicate the relationships between the inductor current (Δi_{dq}) and internal voltage (Δe_{dq}) in the PLL frame and the terminal voltage (Δu_{tdq}) in the synchronous frame, respectively. $G_{pll} = H_{pll}/(s + U^s_{td} H_{pll})$ and $H_{pll} = k_{p,pll} + k_{i,pll}/s$ denotes the compensator of the PLL control, where $k_{p,pll}$ and $k_{i,pll}$ are the proportional and integral gains of the PLL.

The d-axis and q-axis current references can be separately obtained from the DVC and AVC, yielding

$$\Delta i_{dqref} = G_{iu} \Delta u^s_{tdq} + G_{ii} \Delta i^s_{dq} \tag{A.5}$$

$$G_{iu} = \begin{bmatrix} G_{uc} I_{d0} & G_{uc} I_{q0} \\ H_{AVC} & 0 \end{bmatrix} \quad G_{ii} = \begin{bmatrix} G_{uc} U^s_{td} & 0 \\ 0 & 0 \end{bmatrix} \tag{A.6}$$

where $G_{uc} = -(sk_{p,dvc} + k_{i,dvc})/(s^2 C U_{dc0})$, and $H_{AVC} = k_{p,avc} + k_{i,avc}/s$ denotes the AVC compensator. ($k_{p,dvc}$, $k_{i,dvc}$) and ($k_{p,avc}$, $k_{i,avc}$) are the proportional and integral gains of the DVC and AVC, respectively.

Due to the direction of current reference value, the impedance of the VSC can be obtained by

$$Z_{dq} = -\frac{\Delta u_{tdq}}{\Delta i_{dq}} \tag{A.7}$$

By combing (A.1), (A.2), (A.3), and (A.5), it yields the final results in (1) and (2) in the text. For more details, see Refs. [6], [7], [19].

As for the load,

$$Z_L = \frac{\Delta u_{tdq}}{\Delta i_{dq}} \tag{A.8}$$

and the load in Fig. 1 is a single inductance, which can be written as

$$Z_L = \begin{bmatrix} sL_g & -\omega_1 L_g \\ \omega_1 L_g & sL_g \end{bmatrix} \tag{A.9}$$

Combing the impedance of the source (Z_{dq}) and the load (Z_L), the small-signal stability of the system can be determined, as shown in section II-C.

C. STATE SPACE MODEL OF SLOW-SCALE MODEL

Referring to [22], [23], [35], the slow-scale (voltage-timescale) state space model can be established by considering the dynamics of the DVC, AVC, capacitor, and PLL. The state variables can be chosen as follows:

$$\Delta x = [\ \Delta x_1\ \ \Delta x_2\ \ \Delta u_{dc}\ \ \Delta x_3\ \ \Delta\varphi\ ] \tag{A.10}$$

where Δx_1 is the state variables of the DVC, Δx_2 denotes the dynamics of the AVC, Δu_{dc} denotes the dynamics of the capacitor, and Δx_3 and $\Delta\varphi$ are the state variables of the PLL.

The state matrix is:

$$A = \begin{bmatrix} 0 & 0 & k_{i,dvc} & 0 & 0 \\ 0 & \dfrac{-L_g k_{i,avc}}{1+L_g k_{p,avc}} & 0 & 0 & g_{25} \\ \dfrac{-i_{q0}L_g + u_{td0}}{Cu_{dc0}} & g_{32} & g_{33} & 0 & g_{35} \\ \dfrac{L_g k_{i,pll}}{u_{td0}} & 0 & \dfrac{L_g k_{p,dvc} k_{i,pll}}{u_{td0}} & 0 & g_{45} \\ \dfrac{L_g k_{p,pll}}{u_{td0}} & 0 & \dfrac{L_g k_{p,dvc} k_{i,pll}}{u_{td0}} & 1 & g_{55} \end{bmatrix} \tag{A.11}$$

where

$$\begin{cases} g_{25} = \dfrac{-U_g \sin\varphi_0 k_{i,avc}}{1+L_g k_{p,avc}} \\ g_{32} = \dfrac{i_{d0}L_g}{(1+L_g k_{p,avc})Cu_{dc0}} \\ g_{33} = -\dfrac{(u_{td0}+i_{q0}L_g)k_{p,dvc}}{Cu_{dc0}} \\ g_{35} = \dfrac{\frac{i_{d0}U_g \sin\varphi_0}{1+L_g k_{p,avc}} + i_{q0}U_g \cos\varphi_0}{Cu_{dc0}} \\ g_{45} = \dfrac{-U_g \cos\varphi_0 k_{i,pll}}{u_{td0}} \\ g_{55} = \dfrac{-U_g \cos\varphi_0 k_{p,pll}}{u_{td0}} \end{cases} \tag{A.12}$$

$$A = \begin{bmatrix} 0 & 1 & 0 & 0 & 0 & 0 \\ f_{21} & f_{22} & 0 & f_{24} & f_{25} & f_{26} \\ -\dfrac{k_{p,cc}U_g \sin\varphi_0}{L_g+L_f} & -k_{p,cc}i_{q0} & -\dfrac{k_{p,cc}}{L_g+L_f} & 0 & -k_{i,cc} & -k_{p,cc} \\ -\dfrac{k_{p,cc}U_g \cos\varphi_0}{L_g+L_f} & k_{p,cc}i_d & 0 & -\dfrac{k_{p,cc}}{L_g+L_f} & k_{p,cc} & -k_{i,cc} \\ \dfrac{\sin\varphi_0}{L_g+L_f} & i_q & \dfrac{1}{L_g+L_f} & 0 & 0 & 1 \\ \dfrac{U_g \cos\varphi_0}{L_g+L_f} & -i_d & 0 & \dfrac{1}{L_g+L_f} & -1 & 0 \end{bmatrix} \tag{A.14}$$

$$A = \begin{bmatrix} 0 & 0 & \dfrac{-k_{p,dvc}i_{d0}}{Cu_{dc0}} & \dfrac{-k_{p,dvc}i_{q0}}{Cu_{dc0}} & k_{i,dvc} & 0 & 0 & \dfrac{-k_{p,dvc}e_{d0}}{Cu_{dc0}} & \dfrac{-k_{p,dvc}e_{q0}}{Cu_{dc0}} \\ \dfrac{L_g k_{i,cc}k_{p,avc}}{L_g+L_f} & 0 & h_{23} & h_{24} & h_{25} & h_{26} & h_{27} & h_{28} & h_{29} \\ k_{i,cc} & 0 & h_{33} & \dfrac{-k_{p,dvc}k_{p,cc}i_{q0}}{Cu_{dc0}} & k_{p,cc}k_{i,dvc} & -k_{p,cc}i_{q0} & \dfrac{-k_{p,cc}\sin\varphi_0}{(L_g+L_f)U_g} & h_{38} & h_{39} \\ h_{41} & k_{i,cc} & h_{43} & h_{44} & h_{45} & h_{46} & h_{47} & h_{48} & h_{49} \\ 0 & 0 & -\dfrac{i_{d0}}{Cu_{dc0}} & -\dfrac{i_{q0}}{Cu_{dc0}} & 0 & 0 & 0 & \dfrac{-e_{d0}}{Cu_{dc0}} & \dfrac{-e_{q0}}{Cu_{dc0}} \\ h_{61} & \dfrac{k_{i,cc}k_{p,pll}L_g}{(L_g+L_f)U_{t0}} & h_{63} & h_{64} & h_{65} & h_{66} & h_{67} & h_{68} & h_{69} \\ 0 & 0 & 0 & 0 & 0 & 1 & 0 & 0 & 0 \\ 0 & 0 & \dfrac{1}{L_g+L_f} & 0 & 0 & i_{q0} & \dfrac{\sin\varphi_0}{(L_g+L_f)U_{g0}} & 0 & \omega_0 \\ 0 & 0 & 0 & \dfrac{1}{L_g+L_f} & 0 & -i_{d0} & \dfrac{\cos\varphi_0}{L_g+L_f} & -\omega_0 & 0 \end{bmatrix} \tag{A.17}$$

$$
\begin{cases}
h_{23}=\dfrac{k_{i,avc}L_g(L_g+L_f)Cu_{dc0}-k_{p,avc}L_g[k_{p,cc}Cu_{dc0}+(L_g+L_f)k_{p,cc}k_{p,dvc}i_{d0}]}{(L_g+L_f)^2Cu_{dc0}}=h_{24}=-\dfrac{k_{p,dvc}k_{p,avc}k_{p,cc}L_gi_{q0}}{(L_g+L_f)\,Cu_{dc0}}\\
h_{25}=\dfrac{k_{i,dvc}k_{p,avc}k_{p,cc}L_g}{L_g+L_f}\quad h_{26}=-k_{p,avc}\dfrac{U_{g0}L_gk_{p,cc}i_{q0}+L_f\sin\varphi_0}{(L_g+L_f)}\\
h_{27}=-\dfrac{k_{i,avc}L_f\sin\varphi_0}{(L_g+L_f)\,U_{g0}}-\dfrac{k_{p,avc}k_{p,cc}L_g\sin\varphi_0}{(L_g+L_f)^2U_{g0}}\quad h_{28}=-\dfrac{k_{p,avc}L_g\left(k_{i,cc}Cu_{dc0}+k_{p,dvc}k_{p,cc}e_{d0}\right)}{(L_g+L_f)Cu_{dc0}}\\
h_{29}=-\dfrac{k_{p,avc}L_g\left(k_{p,cc}\omega_0Cu_{dc0}+k_{p,dvc}k_{p,cc}e_{q0}\right)}{(L_g+L_f)Cu_{dc0}}\quad h_{33}=-\dfrac{k_{p,cc}}{L_g+L_f}-\dfrac{k_{p,cc}k_{p,dvc}i_{d0}}{Cu_{dc0}}\\
h_{38}=-k_{i,cc}-\dfrac{k_{p,dvc}k_{p,cc}e_{d0}}{Cu_{dc0}}\quad h_{39}=-k_{p,cc}\omega_0-\dfrac{k_{p,dvc}k_{p,cc}e_{q0}}{Cu_{dc0}}\\
h_{41}=\dfrac{k_{p,avc}k_{p,cc}k_{i,cc}L_g}{L_g+L_f}\quad h_{43}=k_{p,cc}L_g\dfrac{k_{i,avc}+k_{p,avc}\left(-\frac{k_{p,cc}}{L_g+L_f}-\frac{k_{p,cc}k_{p,dvc}i_{d0}}{Cu_{dc0}}\right)}{L_g+L_f}\\
h_{44}=-\dfrac{k_{p,cc}}{L_g+L_f}-\dfrac{k_{p,dvc}k_{p,avc}k_{p,cc}^2L_gi_{q0}}{(L_g+L_f)\,Cu_{dc0}}\quad h_{45}=\dfrac{k_{i,dvc}k_{p,avc}k_{p,cc}^2L_g}{L_g+L_f}\\
h_{46}=k_{p,cc}i_{d0}-k_{p,cc}k_{p,avc}\left(\dfrac{k_{p,cc}L_gi_{q0}U_{g0}+L_f\sin\theta_0}{(L_g+L_f)\,U_{g0}}\right)\\
h_{47}=-\dfrac{k_{p,cc}\cos\theta_0}{L_g+L_f}+k_{p,cc}\left(-\dfrac{k_{i,avc}L_f\sin\theta_0}{(L_g+L_f)\,U_{g0}}-\dfrac{k_{p,avc}k_{p,cc}L_g\sin\theta_0}{(L_g+L_f)^2U_{g0}}\right)\\
h_{48}=k_{p,cc}\omega_0-\dfrac{k_{p,avc}k_{p,cc}L_g\left(Cu_{dc}k_{i,cc}+k_{p,dvc}k_{p,cc}e_{d0}\right)}{(L_g+L_f)Cu_{dc}}\quad h_{49}=-k_{i,cc}-\dfrac{k_{p,avc}k_{p,cc}L_g\left(k_{p,cc}\omega_0Cu_{dc}+k_{p,dvc}k_{p,cc}e_{q0}\right)}{(L_g+L_f)Cu_{dc}}\\
h_{61}=\dfrac{k_{p,avc}k_{p,cc}k_{i,cc}k_{p,pll}L_g^2}{(L_g+L_f)^2U_{t0}}\quad h_{63}=\dfrac{k_{p,cc}k_{p,pll}L_g\left(k_{i,avc}L_g+k_{p,avc}L_g\left(-\frac{k_{p,cc}}{L_g+L_f}-\frac{k_{p,cc}k_{p,dvc}i_{d0}}{Cu_{dc0}}\right)\right)}{(L_g+L_f)^2U_{t0}}\\
h_{64}=\dfrac{k_{i,pll}L_g+k_{p,pll}L_g\left(-\frac{k_{p,cc}}{L_g+L_f}-\frac{k_{p,cc}^2k_{p,avc}k_{p,dvc}i_{q0}L_g}{(L_g+L_f)Cu_{dc0}}\right)}{(L_g+L_f)\,U_{t0}}\quad h_{65}=\dfrac{k_{i,dvc}k_{p,avc}k_{p,cc}^2k_{p,pll}L_g^2}{(L_g+L_f)^2U_{t0}}\\
h_{66}=\dfrac{k_{p,pll}\left[L_g\left(k_{p,cc}i_{d0}+k_{p,avc}k_{p,cc}\left(-\frac{k_{p,cc}L_gi_{q0}}{L_g+L_f}-\frac{L_f\sin\varphi_0}{(L_g+L_f)U_{g0}}\right)\right)-L_f\cos\varphi_0\right]}{(L_g+L_f)\,U_{t0}}\\
h_{67}=\dfrac{-k_{i,pll}L_f\cos\varphi_0+k_{p,pll}L_g\left[-\frac{k_{p,cc}\cos\varphi_0}{L_g+L_f}+k_{p,cc}\left(-\frac{k_{i,avc}L_f\sin\varphi_0}{(L_g+L_f)U_{g0}}-\frac{k_{p,avc}k_{p,cc}L_g\sin\varphi_0}{(L_g+L_f)^2U_{g0}}\right)\right]}{(L_g+L_f)\,U_{t0}}\\
h_{68}=k_{p,pll}L_g\dfrac{k_{p,cc}L_g+L_f\omega_0+k_{p,avc}k_{p,cc}L_g\left(-k_{i,cc}-\frac{k_{p,dvc}k_{p,cc}e_{d0}}{Cu_{dc0}}\right)}{(L_g+L_f)^2U_{t0}}\\
h_{69}=k_{p,pll}L_g\dfrac{-k_{i,cc}L_g+L_f+k_{p,avc}k_{p,cc}L_g\left(-k_{p,cc}\omega_0-\frac{k_{p,dvc}k_{p,cc}e_{q0}}{Cu_{dc0}}\right)}{(L_g+L_f)^2U_{t0}}
\end{cases}
\tag{A.18}
$$

D. STATE SPACE MODEL OF FAST-SCALE MODEL

Referring to [6], [27], [33], the fast-scale (current-timescale) state space model can be established by considering the dynamics of the ACC, line inductance, and PLL. The state variables can be chosen as follows:

$$\Delta x=[\,\Delta\varphi\ \ \Delta\omega\ \ \Delta e_d\ \ \Delta e_q\ \ \Delta i_d\ \ \Delta i_q\,] \tag{A.13}$$

where $\Delta\varphi$ and $\Delta\omega$ are the state variables of the PLL, Δe_d and Δe_q are the state variables of the ACC, and Δi_d and Δi_q denote the dynamics of the line inductance.

The state matrix is (A.14), as shown at the bottom of the previous page, with the detailed information in (A.15):

$$
\begin{cases}
f_{21}=-[\dfrac{k_{p,pll}k_{p,cc}L_g}{(L_g+L_f)^2}+\dfrac{k_{i,pll}L_f}{L_g+L_f}]U_g\cos\varphi_0\\
f_{22}=\dfrac{k_{p,cc}k_{p,pll}L_gi_{d0}}{L_g+L_f}-\dfrac{k_{p,pll}L_fU_g\cos\varphi_0}{L_g+L_f}\\
f_{24}=\dfrac{k_{i,pll}L_g}{L_g+L_f}-\dfrac{k_{p,pll}k_{p,cc}L_g}{(L_g+L_f)^2}\\
f_{25}=\dfrac{k_{p,cc}k_{p,pll}L_g}{L_g+L_f}\\
f_{26}=-\dfrac{k_{p,pll}L_gk_{i,cc}}{L_g+L_f}
\end{cases}
\tag{A.15}
$$

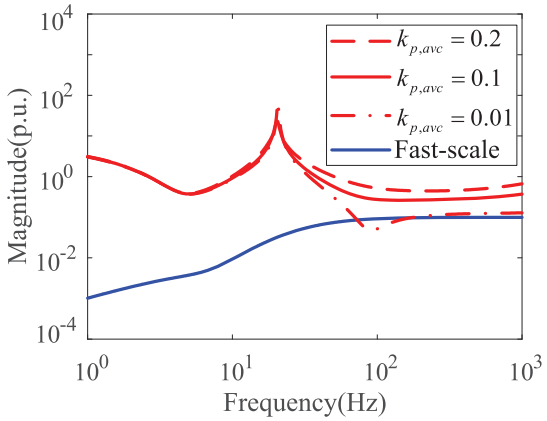

FIGURE 21. Plots of the Z_{qd} 's amplitude responses of the full-scale (red lines) and fast-scale impedance (blue solid line) for different $k_{p,avc}$'s.

E. STATE SPACE MODEL OF FULL-SCALE MODEL

Referring to [8], [16], [38], the full-scale state space model can be established by considering the dynamics of the ACC, line inductance, AVC, DVC, and PLL. The state variables can be chosen as follows:

$$\Delta x = [\,\Delta i_{dref}\ \ \Delta i_{qref}\ \ \Delta e_d\ \ \Delta e_q\ \ \Delta u_{dc}\ \ \Delta\omega \quad \Delta\varphi\ \ \Delta i_d\ \ \Delta i_q\,] \tag{A.16}$$

where Δi_{dref} and Δu_{dc} denote the dynamics of the DVC and the capacitor, respectively, Δi_{qref} is the state variable of the AVC, Δe_d and Δe_q denote the dynamics of the ACC, $\Delta\varphi$ and $\Delta\omega$ are the state variables of the PLL, and Δi_d and Δi_q denote the dynamics of the line inductance.

The state matrix is (A.17), as shown at the bottom of the 13th page, with the detailed information in (A.18), as shown at the top of the previous page. Therefore, the eigenvalues of these models in Tab. 1 can be obtained by the modal analysis.

F. EXPLANATION FOR THE MISMATCH IN Z_{qd}

The small mismatch of Z_{qd} in Fig. 3 is discussed here. According to the Bode responses, this mismatch can hardly be narrowed by changing all of the parameters except for the proportional coefficient of the AVC ($k_{p,avc}$). The amplitude responses of Z_{qd} with the changing of $k_{p,avc}$ are shown in Fig. 21. It can be seen that the mismatch between the fast-scale and full-scale impedance (Z_{qd}) in high frequency range decreases with the decrease of $k_{p,avc}$.

G. DQ-IMPEDANCE MODEL WITH ONLY DVC OUTER CONTROL

The d-axis current reference is obtained from the DVC and the q-axis current reference is set to constant ($H_{AVC} = 0$). G_{ii} is same as (A.6), but G_{iu} becomes

$$G_{iu} = \begin{bmatrix} G_{uc}I_{d0} & G_{uc}I_{q0} \\ 0 & 0 \end{bmatrix} \tag{A.19}$$

H. DQ-IMPEDANCE MODEL WITH PC OUTER CONTROL

Linearizing (21) and substituting it into (A.5), we have

$$G_{iu} = -\begin{bmatrix} I_{d0}H_p & I_{q0}H_p \\ I_{q0}H_q & -I_{d0}H_q \end{bmatrix} \quad G_{ii} = -U_{td}^s \begin{bmatrix} H_p & 0 \\ 0 & H_q \end{bmatrix} \tag{A.20}$$

where H_p and H_q separately denote active and reactive PC compensator transfer functions.

REFERENCES

[1] Y. Chi, B. Tang, J. Hu, X. Tian, H. Tang, Y. Li, S. Sun, L. Shi, and L. Shuai, "Overview of mechanism and mitigation measures on multi-frequency oscillation caused by large-scale integration of wind power," *CSEE J. Power Energy Syst.*, vol. 5, no. 4, pp. 433–443, 2019.
[2] Z. Yang, S. Cheng, and M. Zhan, "Problems and challenges of power-electronic-based power system stability: A case study of transient stability comparison," (in Chinese), *Acta Phys. Sinica*, vol. 69, no. 8, pp. 1–14, 2020.
[3] X. Yuan, S. Cheng, and J. Hu, "Multi-time scale voltage and power angle dynamics in power electronics dominated large power systems," (in Chinese), *Proc. CSEE*, vol. 36, no. 19, pp. 5145–5154, 2016.
[4] X. Yuan, "Overview of problems in large-scale wind integrations," *J. Mod. Power Syst. Clean Energy*, vol. 1, no. 1, pp. 22–25, Jun. 2013.
[5] Y. Wang, X. Wang, Z. Chen, and F. Blaabjerg, "Small-signal stability analysis of inverter-fed power systems using component connection method," *IEEE Trans. Smart Grid*, vol. 9, no. 5, pp. 5301–5310, Sep. 2018.
[6] J. Sun, "Impedance-based stability criterion for grid-connected inverters," *IEEE Trans. Power Electron.*, vol. 26, no. 11, pp. 3075–3078, Nov. 2011.
[7] L. Harnefors, M. Bongiorno, and S. Lundberg, "Input-admittance calculation and shaping for controlled voltage-source converters," *IEEE Trans. Ind. Electron.*, vol. 54, no. 6, pp. 3323–3334, Dec. 2007.
[8] N. Pogaku, M. Prodanović, and T. C. Green, "Modeling, analysis and testing of autonomous operation of an inverter-based microgrid," *IEEE Trans. Power Electron.*, vol. 22, no. 2, pp. 613–625, Mar. 2007.
[9] N. R. Chaudhuri, R. Majumder, B. Chaudhuri, and J. Pan, "Stability analysis of VSC MTDC grids connected to multimachine AC systems," *IEEE Trans. Power Del.*, vol. 26, no. 4, pp. 2774–2784, Oct. 2011.
[10] W. Du, Q. Fu, and H. Wang, "Small-signal stability of an AC/MTDC power system as affected by open-loop modal coupling between the VSCs," *IEEE Trans. Power Syst.*, vol. 33, no. 3, pp. 3143–3152, May 2018.
[11] Y. Xu, M. Zhang, L. Fan, and Z. Miao, "Small-signal stability analysis of type-4 wind in series-compensated networks," *IEEE Trans. Energy Convers.*, vol. 35, no. 1, pp. 529–538, Mar. 2020.
[12] Y. Li, L. Fan, and Z. Miao, "Wind in weak grids: Low-frequency oscillations, subsynchronous oscillations, and torsional interactions," *IEEE Trans. Power Syst.*, vol. 35, no. 1, pp. 109–118, Jan. 2020.
[13] H. Wu, X. Wang, and L. H. Kocewiak, "Impedance-based stability analysis of voltage-controlled MMCs feeding linear AC systems," *IEEE J. Emerg. Sel. Topics Power Electron.*, vol. 8, no. 4, pp. 4060–4074, Dec. 2020.
[14] S. Shah and L. Parsa, "Impedance modeling of three-phase voltage source converters in DQ, sequence, and phasor domains," *IEEE Trans. Energy Convers.*, vol. 32, no. 3, pp. 1139–1150, Sep. 2017.
[15] A. Rygg, M. Molinas, C. Zhang, and X. Cai, "On the equivalence and impact on stability of impedance modeling of power electronic converters in different domains," *IEEE J. Emerg. Sel. Topics Power Electron.*, vol. 5, no. 4, pp. 1444–1454, Dec. 2017.
[16] X. Wang, L. Harnefors, and F. Blaabjerg, "Unified impedance model of grid-connected voltage-source converters," *IEEE Trans. Power Electron.*, vol. 33, no. 2, pp. 1775–1787, Feb. 2018.
[17] L. Huang, H. Xin, Z. Li, P. Ju, H. Yuan, Z. Lan, and Z. Wang, "Grid-synchronization stability analysis and loop shaping for PLL-based power converters with different reactive power control," *IEEE Trans. Smart Grid*, vol. 11, no. 1, pp. 501–516, Jan. 2020.
[18] M. Beza and M. Bongiorno, "Impact of converter control strategy on low- and high-frequency resonance interactions in power-electronic dominated systems," *Int. J. Electr. Power Energy Syst.*, vol. 120, Sep. 2020, Art. no. 105978.
[19] B. Wen, D. Boroyevich, R. Burgos, P. Mattavelli, and Z. Shen, "Analysis of D-Q small-signal impedance of grid-tied inverters," *IEEE Trans. Power Electron.*, vol. 31, no. 1, pp. 675–687, Jan. 2016.

[20] Y. Tu, J. Liu, Z. Liu, D. Xue, and L. Cheng, "Impedance-based analysis of digital control delay in grid-tied voltage source inverters," *IEEE Trans. Power Electron.*, vol. 35, no. 11, pp. 11666–11681, Nov. 2020.

[21] J. Sun, I. Vieto, E. V. Larsen, and C. Buchhagen, "Impedance-based characterization of digital control delay and its effects on system stability," in *Proc. 20th Workshop Control Modeling Power Electron. (COMPEL)*, Jun. 2019, pp. 1–8.

[22] Z. Yang, R. Ma, S. Cheng, and M. Zhan, "Nonlinear modeling and analysis of grid-connected voltage-source converters under voltage dips," *IEEE J. Emerg. Sel. Topics Power Electron.*, vol. 8, no. 4, pp. 3281–3292, Dec. 2020.

[23] Y. Huang, D. Wang, L. Shang, G. Zhu, H. Tang, and Y. Li, "Modeling and stability analysis of DC-link voltage control in multi-VSCs with integrated to weak grid," *IEEE Trans. Energy Convers.*, vol. 32, no. 3, pp. 1127–1138, Sep. 2017.

[24] Y. Huang, X. Zhai, J. Hu, D. Liu, and C. Lin, "Modeling and stability analysis of VSC internal voltage in DC-link voltage control timescale," *IEEE J. Emerg. Sel. Topics Power Electron.*, vol. 6, no. 1, pp. 16–28, Mar. 2018.

[25] X. Quan, X. Lin, Y. Zheng, and Y. Kang, "Transient stability analysis of grid-connected converter driven by imbalance power under non-severe remote voltage sag," *Energies*, vol. 14, no. 6, p. 1737, Mar. 2021.

[26] Y. Gu, N. Bottrell, and T. C. Green, "Reduced-order models for representing converters in power system studies," *IEEE Trans. Power Electron.*, vol. 33, no. 4, pp. 3644–3654, Apr. 2018.

[27] R. Ma, Z. Yang, S. Cheng, and M. Zhan, "Sustained oscillations and bifurcations in three-phase voltage source converter tied to AC grid," *IET Renew. Power Gener.*, vol. 14, no. 18, pp. 3770–3781, Dec. 2020.

[28] D. Dai, S. Li, X. Ma, and C. K. Tse, "Slow-scale instability of single-stage power-factor-correction power supplies," *IEEE Trans. Circuits Syst. I, Reg. Papers*, vol. 54, no. 8, pp. 1724–1735, Aug. 2007.

[29] X. Xiong, C. K. Tse, and X. Ruan, "Bifurcation analysis and experimental study of a multi-operating-mode photovoltaic-battery hybrid power system," *IEEE J. Emerg. Sel. Topics Circuits Syst.*, vol. 5, no. 3, pp. 316–325, Sep. 2015.

[30] W. Zheng, J. Hu, and X. Yuan, "Analytic quantification of interactions in MTDC systems based on self-/en-stabilizing coefficients in DC voltage control timescale," *IEEE J. Emerg. Sel. Topics Power Electron.*, vol. 9, no. 3, pp. 2980–2991, Jun. 2021.

[31] M. Zhang, X. Yuan, and J. Hu, "Path series expansion method based on self-/en-stabilizing properties and its application in the stability analysis of power systems with diversified power electronic devices," (in Chinese), *Proc. CSEE*, vol. 41, no. 5, pp. 1637–1654, 2021.

[32] J. Ying, X. Yuan, J. Hu, and W. He, "Impact of inertia control of DFIG-based WT on electromechanical oscillation damping of SG," *IEEE Trans. Power Syst.*, vol. 33, no. 3, pp. 3450–3459, May 2018.

[33] Y. Yan, X. Yuan, and J. Hu, "Stationary-frame modeling of VSC based on current-balancing driven internal voltage motion for current control timescale dynamic analysis," *Energies*, vol. 11, no. 2, p. 374, Feb. 2018.

[34] J. Hu, H. Yuan, and X. Yuan, "Modeling of DFIG-based WTs for small-signal stability analysis in DVC timescale in power electronized power systems," *IEEE Trans. Energy Convers.*, vol. 32, no. 3, pp. 1151–1165, Sep. 2017.

[35] Z. Yang, C. Mei, S. Cheng, and M. Zhan, "Comparison of impedance model and amplitude–phase model for power- electronics-based power system," *IEEE J. Emerg. Sel. Topics Power Electron.*, vol. 8, no. 3, pp. 2546–2558, Sep. 2020.

[36] F. Umbría, J. Aracil, F. Gordillo, F. Salas, and J. A. Sánchez, "Three-time-scale singular perturbation stability analysis of three-phase power converters," *Asian J. Control*, vol. 16, no. 5, pp. 1361–1372, Sep. 2014.

[37] F. Umbria, J. Aracil, and F. Gordillo, "Singular perturbation stability analysis of three phase two-level power converters," in *Proc. 18th Medit. Conf. Control Automat. (MED)*, Jun. 2010, pp. 123–128.

[38] X. Wang and F. Blaabjerg, "Harmonic stability in power electronic-based power systems: Concept, modeling, and analysis," *IEEE Trans. Smart Grid*, vol. 10, no. 3, pp. 2858–2870, May 2019.

RUI MA received the B.S. degree in electrical engineering from North China Electronic Power University, Baoding, China, in 2018. He is currently pursuing the Ph.D. degree in electrical engineering with the State Key Laboratory of Advanced Electromagnetic Engineering and Technology, School of Electrical and Electronic Engineering, Huazhong University of Science and Technology, Wuhan, China.

His research interests include the stability and control of renewable energy dominated power systems, such as wide bandwidth oscillations and transient synchronous stability of power systems.

QI QIU was born in Fuzhou, Jiangxi, China, in 1997. He received the B.S. degree from North China Electronic Power University, Baoding, China, in 2018. He is currently pursuing the M.Eng. degree in electrical engineering with the State Key Laboratory of Advanced Electromagnetic Engineering and Technology, School of Electrical and Electronic Engineering, Huazhong University of Science and Technology.

His research interests include stability and control of power systems with renewable energy generation, such as impedance model, harmonic linearization, and small signal stability analysis.

JÜRGEN KURTHS received the Ph.D. degree from the GDR Academy of Sciences, Berlin, Germany, in 1983.

From 1994 to 2008, he was a Full Professor with the University of Potsdam, Potsdam, Germany. Since 2008, he has been a Professor of nonlinear dynamics with the Humboldt University of Berlin, Berlin, and the Chair of the research domain Transdisciplinary Concepts of the Potsdam Institute for Climate Impact Research, Potsdam. He has authored or coauthored more than 600 articles that are cited more than 42 000 times (H-index: 91). His current research interests include synchronization, complex networks, and time-series analysis and their applications. He became a member of the Academy of Europe, in 2010, conferred eight honorary doctorates. He was a recipient of the Richardson Award of the European Geophysical Union, in 2013. He is the Editor-in-Chief of *CHAOS*. He is a Highly Cited Researcher in engineering and physics.

MENG ZHAN (Member, IEEE) was born in Jingdezhen, Jiangxi, China, in 1974. He received the B.S. degree in physics and the Ph.D. degree in nonlinear physics from Beijing Normal University, Beijing, China, in 1996 and 2001, respectively.

From 2001 to 2006, he was a Postdoctoral Researcher with the National University of Singapore, Singapore, and the University of Toronto, Canada. After working as a Full Professor with the Wuhan Institute of Physics and Mathematics, Chinese Academy of Sciences, from 2006 to 2015, recently he joined the State Key Laboratory of Advanced Electromagnetic Engineering and Technology, School of Electrical and Electronic Engineering, Huazhong University of Science and Technology. He has long been engaged in the study of nonlinear dynamics theory of complex systems in multiple directions, such as coupled nonlinear systems, chaos synchronization and control, pattern formation, and complex network dynamics. He has published nearly 100 SCI articles in internationally peer-reviewed journals. His research interests include power system stability, power-electronics-based power system dynamics, and nonlinear analysis of power systems.